Standard Model Baryon Number Violation at Zero Temperature from Higgs Bubble Collisions

Nabeen Bhusal,[1] Simone Blasi,[1,*] Martina Cataldi,[1,2] Aleksandr Chatrchyan,[3,4] Marco Gorghetto,[1] and Géraldine Servant[1,2]

[1]*Deutsches Elektronen-Synchrotron DESY, Notkestraße 85, 22607 Hamburg, Germany*
[2]*II. Institute of Theoretical Physics, Universität Hamburg, 22761 Hamburg, Germany*
[3]*Nordita, KTH Royal Institute of Technology and Stockholm University, Hannes Alfvéns väg 12, SE-106 91 Stockholm, Sweden*
[4]*The Oskar Klein Centre for Cosmoparticle Physics, Department of Physics, Stockholm University, AlbaNova, 10691 Stockholm, Sweden*

(Received 11 September 2025; revised 15 December 2025; accepted 17 April 2026; published 18 June 2026)

We compute for the first time baryon number violation at zero temperature from Higgs bubble collisions and find that it can be of the same order as that from thermal sphalerons in the symmetric phase at electroweak temperatures. We study the dependence of the rate of Chern-Simons number transitions on the shape of the scalar potential and on the Lorentz factor of the bubble walls at collision via large-scale $(3+1)$D lattice simulations of the Higgs doublet and $SU(2)$ gauge fields. We estimate the resulting baryon asymmetry assuming some CP-violating source activated by the Higgs-field variation during the phase transition.

DOI: 10.1103/fv7q-vsbn

Introduction—Baryon number (B) is a global symmetry of the Standard Model (SM) whose violation has never been observed experimentally. It is however efficiently violated by the chiral anomaly at high temperature T through $SU(2)$ vacuum transitions producing integer Chern-Simons (CS) number variations $\Delta N_{\rm CS} \propto \Delta B$, the sphaleron processes, which play a key role in essentially all models of baryogenesis, whether at the electroweak scale [1] or well beyond, as in leptogenesis [2,3]. These transitions can also occur at zero temperature when the Higgs field is driven far from equilibrium, e.g., if the SM electroweak phase transition (EWPT) is quenched, i.e., happens much faster than when thermally induced. This has been exploited in models of (local) *cold* baryogenesis where inflation takes place at the EW scale and the inflaton coupling to the Higgs quenches the Higgs mass parameter, leading to a tachyonic instability that triggers $\Delta N_{\rm CS} \neq 0$ at every point in space [4–9]. The rate of B violation from such a quenched EW crossover (i.e., not first-order EWPT) has been studied on the lattice in [10–21].

In this Letter, we compute for the first time the rate of B violation at $T = 0$ arising from Higgs bubble collisions. We show that this new source of B violation can be of the same order as the one from thermal sphalerons. This opens up the possibility for a new mechanism of EW baryogenesis in models where the reheat temperature associated with a first-order EWPT never exceeds the 130 GeV sphaleron freeze-out temperature [22]. In this context, EW baryogenesis could be potentially realized even for very strongly first order supercooled EWPT, i.e., for bubble wall velocity exceeding the speed of sound, a regime where the standard nonlocal EW baryogenesis charge transport mechanism is highly suppressed [23]. Such frameworks are particularly motivated in composite Higgs models where a light dilaton drives the EWPT [24–30]. See also Refs. [31–34] for baryogenesis with ultrarelativistic walls but additional sources of B violation. More generally, this new source of B violation may impact common models of EW baryogenesis as a new source of B washout.

The production of CS number in this Letter can be attributed to the dynamics of the electroweak textures. These are configurations where the scalar field is in the vacuum manifold $M = SU(2) \times U(1)/U(1)$ everywhere in space, but defines a nontrivial map from M onto the three-sphere $S^3 = \mathbb{R}^3 \cup \{\infty\}$, and are classified by a third homotopy group $\pi_3(M) = \mathbb{Z}$. Thus, the energy of a texture is entirely due to the field gradient. In this Letter, we consider $SU(2)$ as a simplified version of the SM gauge group, i.e., we set the hypercharge gauge coupling $g' = 0$, as this captures the main physics of interest. Textures can arise from the different $SU(2)$-phase orientations of the

*Contact author: simone.blasi@desy.de

Published by the American Physical Society under the terms of the Creative Commons Attribution 4.0 International license. Further distribution of this work must maintain attribution to the author(s) and the published article's title, journal citation, and DOI. Funded by SCOAP³.

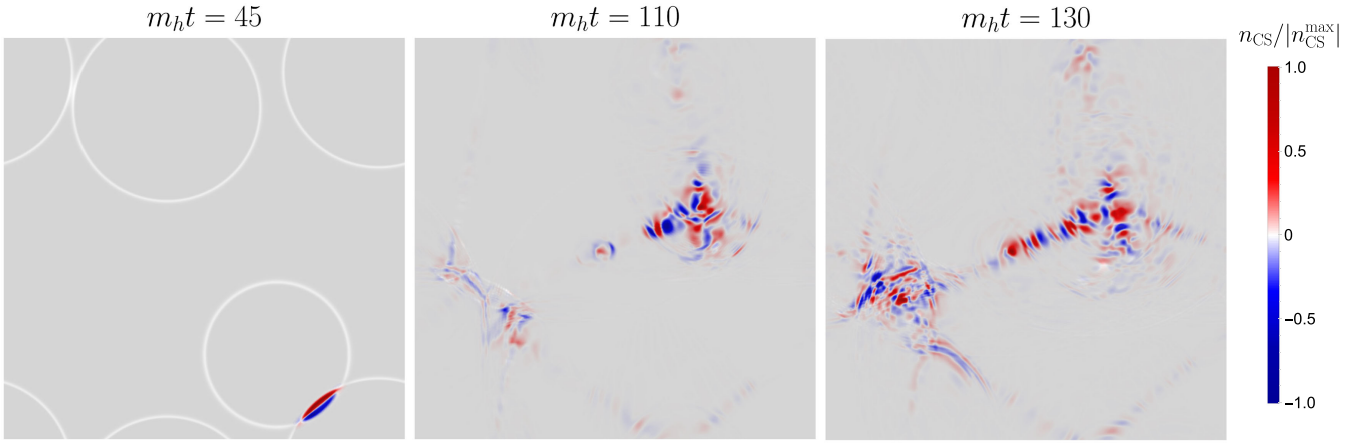


FIG. 1. Snapshots of a two-dimensional slice of the Chern-Simons number density n_{CS} (red/blue) produced in our $(3+1)$D simulations from the collision of Higgs bubble walls (white), defined by $N_{CS}(t) = \int d^3x n_{CS}(t,x)$, where $n_{CS} = (g^2/16\pi^2)\epsilon^{ijk}\mathrm{Tr}[W_i W_{jk} + \frac{2}{3} i g W_i W_j W_k]$, for the potential degeneracy parameter $\epsilon = 0.32$, normalized to its maximum value over the slice $n_{CS}^{max}(t)$. For an animation, see Ref. [38].

Higgs doublet ϕ across space after spontaneous symmetry breaking. A texture is labeled by the (integer) Higgs winding number $N_W = (1/24\pi^2)\int d^3x \epsilon_{ijk}\mathrm{Tr}(\partial_i\Phi)\Phi^\dagger \times (\partial_j\Phi)\Phi^\dagger(\partial_k\Phi)\Phi^\dagger$, where $\Phi = (i\sigma_2\phi^*, \phi)/|\phi|^2 \in SU(2)$, and the gauge field Chern-Simons number $N_{CS}(t) - N_{CS}(0) = (g^2/16\pi^2)\int_0^t dt' \int d^3x \mathrm{Tr}[W^{\mu\nu}\tilde{W}_{\mu\nu}]$, where the dual of the $SU(2)$ field strength $W^{\mu\nu}$ is $\tilde{W}_{\mu\nu} = \frac{1}{2}\epsilon_{\mu\nu\rho\sigma}W^{\rho\sigma}$. A prototypical texture with $N_W = 1$ has $W_{\mu\nu} = 0$ and $\phi(x) = e^{-i\eta(r)x_i\sigma_i/r}(0, v)$, where $\eta(r) = \pi\tanh(r/r_t)$, σ_i are Pauli matrices, $v = 246$ GeV is the Higgs expectation value, and r_t is the radius. The minimal-energy (vacuum) configuration has $N_{CS} = N_W$, while a texture has $N_{CS} - N_W \neq 0$. Textures with characteristic length scale smaller than the inverse W mass m_W^{-1} decay by changing N_W, while those larger than m_W^{-1} get "dressed" by the gauge fields and decay by altering N_{CS} [35]. Thus, crucially, the formation and subsequent decay of $SU(2)$ textures can lead to a change in the CS number ΔN_{CS}, which eventually leads to baryon number production via the quantum anomaly, $\Delta B = N_F \Delta N_{CS}$, where $N_F = 3$ is the number of flavors.

Higgs bubble collisions generate Higgs inhomogeneities that produce N_W and N_{CS}, possibly directly or through formation and decay of textures. Our simulations indeed observe such production, see Fig. 1. To quantify the change in the CS number, we define the CS number diffusion rate

$$\Gamma_{CS} = \frac{1}{L^3}\frac{d\Delta N_{CS}^2(t)}{dt} \equiv \frac{d\Delta n_{CS}^2(t)}{dt}, \tag{1}$$

with Chern-Simons variance

$$\Delta N_{CS}^2(t) \equiv \langle N_{CS}^2(t)\rangle - \langle N_{CS}(t)\rangle^2 \tag{2}$$

where $\langle . \rangle$ is the statistical average over realizations and L^3 is the volume. Notice that $\langle N_{CS}\rangle = 0$, as we do not include sources of CP violation. It will be useful to compare Eq. (1) with the SM thermal sphaleron rate in the symmetric phase [22,36,37], $\Gamma_{th} \sim 25\alpha_w^5 T^4$, and with the rate from a quenched EW crossover [4,11,12], $\Gamma_{tach} \equiv \alpha_w^4 T_{eff}^4$, where T_{eff} parametrizes the efficiency of baryon number violation induced by the tachyonic instability and depends on the amount of quenching of the EW crossover.

Real-time simulations—We rely on SM physics only, except that we assume a first-order EWPT triggered by a new light scalar, with the Higgs field tracking its bubble profile. For simplicity, however, we model the transition using a modified single-field Higgs potential in which $\phi = 0$ is a local minimum, see Supplemental Material I [39] and Refs. [40–42]. We solve the Higgs and gauge boson equations of motion numerically (see also Ref. [43]) on a periodic cubic grid with $N_x^3 \in [500^3 - 1500^3]$ points, setting $m_W^2/m_h^2 = 0.4$ as in the SM (neglecting hypercharge). We expect our main results on the CS rate to be barely affected when the full $SU(2) \times U(1)$ is considered. The main model-dependent parameter is the degeneracy parameter ϵ, which characterizes the scalar potential shape, and plays an important role in the field dynamics during and after bubble collisions [25,44,45]. It is defined by $\epsilon = (V_{barr}/V_{barr} + |\Delta V|) \in (0,1)$, where V_{barr} is the barrier height and ΔV is the energy difference between the $\phi = 0$ and $\phi = v/\sqrt{2}$ vacua [44]. We have $\epsilon \to 1$ for degenerate vacua, $|\Delta V| \ll V_{barr}$, and $\epsilon \to 0$ for nondegenerate vacua, $|\Delta V| \gg V_{barr}$. For large ϵ, the walls tend to reflect upon collision, temporarily recreating a region of false vacuum that eventually shrinks after a several iterations. Instead, for $\epsilon \ll 1$ the barrier is not effective in trapping the field in the

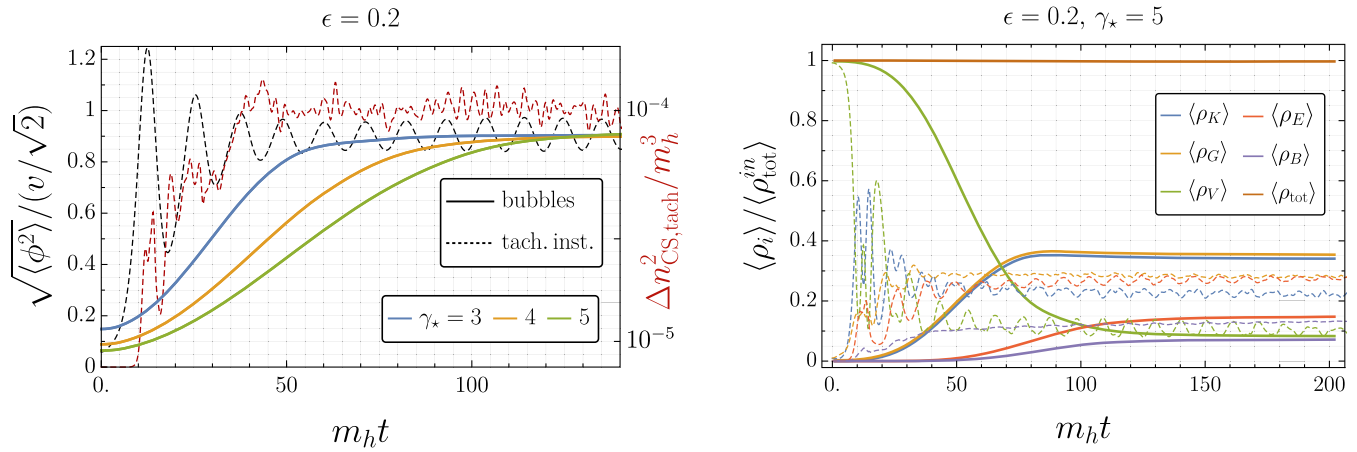


FIG. 2. Solid lines indicate bubble collisions, whereas dashed lines represent a typical tachyonic transition with an instantaneous quench (Higgs field rolling down its $T = 0$ potential from the origin). Left: Time evolution of volume-averaged Higgs norm during the phase transition in units of its value today $v = 246$ GeV, for different values of Lorentz-factor $\gamma_\star$ of the walls at collision. The dashed red line is the CS variance for the tachyonic transition. Right: Evolution of the energy density components normalized by the total initial energy density $\rho^{\rm in}_{\rm tot}$. The scalar kinetic and gradient, and $SU(2)$ electric and magnetic energies are: $\rho_K = |\dot\phi|^2, \rho_G = |D_i\phi|^2, \rho_E = \frac{1}{2}W_{0i}W_{0i}, \rho_B = W^a_{jk}W^a_{jk}$; ρ_V is the potential. We use a degeneracy parameter $\epsilon = 0.2$, and averaged over 30 simulations in both panels.

false vacuum, and the true minimum is eventually reached after just a few oscillations.

We nucleate $N_b = 10$ bubbles simultaneously, but verify that our results are independent of N_b, see Supplemental Material I [39]. Their profile $h_c(r)$ is the $O(4)$ solution of the equations of motion characterized by a critical radius R_c and wall width l_0, with $R_c > l_0 \sim m_h^{-1}$. Contrary to tachyonic instability studies, no (quantum) fluctuations are introduced. Bubbles are nucleated with a random position and orientation θ_i in the $SU(2)$ space: $\phi = \frac{1}{\sqrt{2}} e^{-i\theta_i\sigma_i}[0, h_c(r)]$. The different orientations allow the scalar field to acquire a nonzero winding number, generating a current that ultimately sources the gauge fields (initially set to zero), $D_\mu W^{\mu\nu} = 2g\,\mathrm{Im}(\phi^\dagger D^\mu\phi)$. After collision, bubbles fill the whole volume with the true vacuum. Defining the bubble radius at collision $R_\star = \gamma_\star R_c$, we estimate the Lorentz factor of the wall at collision, $\gamma_\star$, via $L^3 \sim N_b(2/\sqrt{3})^3(4\pi/3)(R_c\gamma_\star)^3$. Figure 2 (left) shows the time evolution of the volume-averaged Higgs norm during the transition, for varying $\gamma_\star$. Our analysis applies to EW bubbles that collide in the runaway regime, see section Runaway bubbles of the End Matter.

The evolution of the volume-averaged energy density components normalized by the initial total energy $\rho^{\rm in}_{\rm tot}$ is shown in Fig. 2 (right) ($\rho_{\rm tot}$ is conserved). Most of the potential energy is converted into Higgs kinetic and gradient energy, with a non-negligible fraction transferred to electric and magnetic fields. This picture does not change notably for different values of ϵ from what shown in Fig. 2.

Nonzero N_W and $N_{\rm CS}$ are produced as the bubbles collide (see Fig. 1). Once the phase transition completes, $N_{\rm CS}$ relaxes toward N_W in the vacuum configuration; see Fig. 5 in the End Matter for an example. Note that the collision of only two bubbles does not produce N_W due to the cylindrical symmetry. The CS variance $\Delta n^2_{\rm CS,tach}$ in the original cold baryogenesis from a tachyonic instability with instantaneous quench is shown for comparison in Fig. 2 (left).

Dependence of Chern-Simons rate on $\gamma_\star$ and ϵ—We study the dependence of the CS rate, $\Gamma_{\rm CS}$, on the EWPT parameters: (i) $\gamma_\star$, the average Lorentz-boost factor of the bubble walls at collision, which in a cosmological context is proportional to β/H, where β^{-1} is the phase transition duration and H is the Hubble parameter; (ii) the degeneracy parameter ϵ, encoding the potential shape and the dynamics of bubble wall collisions. We perform simulations varying $\gamma_\star$ (via changing L and thus $R_\star$), and for several values of ϵ, with $N_b = 10$ and $l_\star/dx \gtrsim 2$ points per bubble wall (see Supplemental Material I [39] for details). The statistical average in Eq. (2) is done over 30 independent simulations. Our results for $\Gamma_{\rm CS}$ have to be extrapolated to the physical limit of large $\gamma_\star$, or small β/H, for which there is a large hierarchy between the bubble size and the microscopic scale set by the Higgs mass. We are able to test values of $\gamma_\star \lesssim 8$, and since $HR_\star = \gamma_\star HR_c = (8\pi)^{1/3} v_w (\beta/H)^{-1}$ with $H \sim v^2/M_{\rm Pl}$ and $v_w \sim 1$ the wall velocity, this corresponds to $\beta/H \gtrsim 10^{15}$, which are much larger than the typical ones for a strong first-order PT, namely $\beta/H \sim 10^1$–10^3.

In Fig. 3 (left) we show the time evolution of the CS variance, $\Delta n^2_{\rm CS}$, and the CS rate $\Gamma_{\rm CS}$, defined by Eqs. (1), (2), for $\epsilon = 0.32$. At a fixed ϵ, the CS variance may be parametrized by

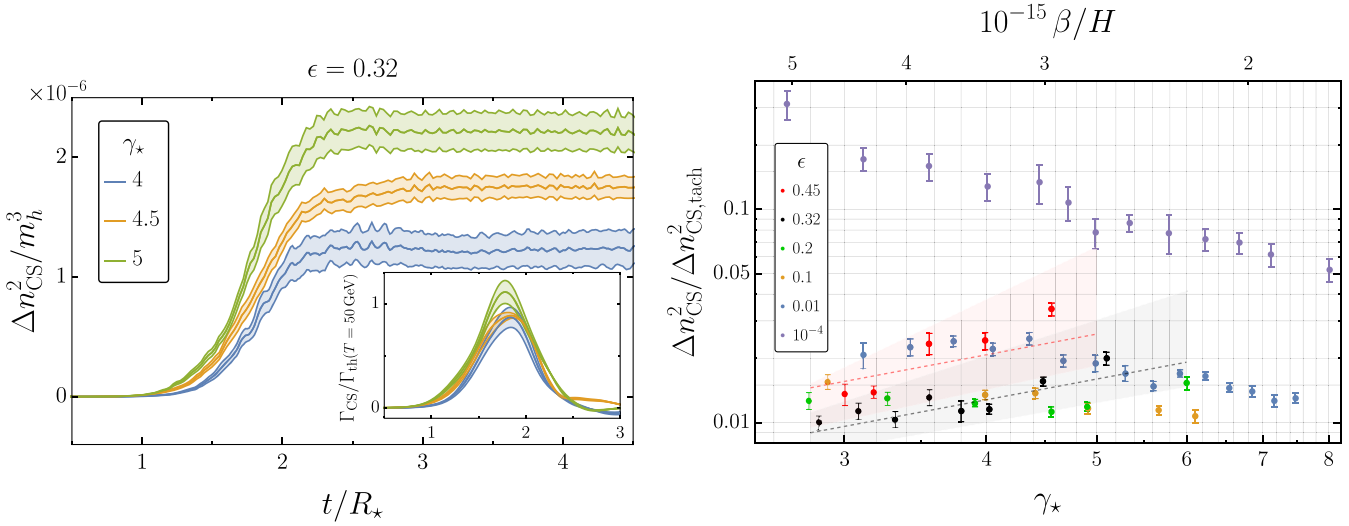


FIG. 3. Left: evolution of Chern-Simons variance $\Delta n^2_{\rm CS}$ and rate $\Gamma_{\rm CS}$ as a function of $\gamma_\star$, for $\epsilon = 0.32$. For each $\gamma_\star = \{4, 4.5, 5\}$, we have $m_h R_\star = \{80, 90, 100\}$. Right: asymptotic value of CS variance $\Delta n^2_{\rm CS}$ as a function of the Lorentz-boost factor $\gamma_\star$ at collision, for different values of ϵ, normalized by the CS variance from a tachyonic instability, $\Delta n^2_{\rm CS,tach} = 10^{-4} m_h^3$ [14,18]. While for $\epsilon \ll 1$ the CS variance appears to decrease with $\gamma_\star$, for $\epsilon \gtrsim 0.3$ there is some evidence that it increases $\propto \gamma_\star^a$ with $a \gtrsim 1$ (e.g., black and red). This corresponds to a nondecreasing $\Gamma_{\rm CS}$ with respect to $\gamma_\star$ (inset in the left panel) and hints at a large baryon number violation at the physical point $\gamma_\star \gg 1$.The bands denote the 2σ error on the fitted exponent a; for comparison, the dashed line corresponds to $a = 1$, still consistent with the data.

$$\Delta n^2_{\rm CS} = c \times \gamma_\star^a f(t/R_\star), \tag{3}$$

where c is a constant, the exponent a encodes the possibility of a dependence on $\gamma_\star$, either increasing or decreasing, f is the profile observed in Fig. 3. In a timescale set by the completion of the EWPT, $\mathcal{O}(R_\star)$, the CS variance has grown to a sizable value $\Delta n^2_{\rm CS}/m_h^3 \sim 10^{-6}$. This value corresponds to $\Gamma_{\rm CS}$ being roughly of the same order as the thermal sphaleron rate in the symmetric phase, $\Gamma_{\rm th}$, at $T \sim 50$ GeV, active for the whole duration of the transition, see inset of Fig. 3 (left). Despite the small range of $\gamma_\star$ considered for this value of ϵ, as we discuss next, we see some indication for a dependence compatible with $a = 1$ in Eq. (3). Since $\Gamma_{\rm CS} \propto \gamma_\star^{a-1}$, this would suggest that the (peak of the) CS rate approaches a constant at $\gamma_\star \gg 1$ for this large ϵ, see the inset. The characteristic timescale is associated with B violation, when $\Gamma_{\rm CS} \neq 0$, is $\sim R_\star$, reaching macroscopic values (i.e., fractions of Hubble time), in contrast with the tachyonic instability in original cold baryogenesis where the relevant timescale is the time of equilibration of the Higgs modes, which is microscopic.

In Fig. 3 (right) we show the asymptotic value of $\Delta n^2_{\rm CS}$ after the EWPT completes as a function of $\gamma_\star$ for different ϵ, normalized to the variance from a tachyonic phase transition, $\Delta n^2_{\rm CS,tach}$, shown in Fig. 2 for comparison. For small $\epsilon \lesssim 0.1$, $\Delta n^2_{\rm CS}$ decreases with $\gamma_\star$ (or equivalently $R_\star$), namely $a < 0$ in Eq. (3). For $\epsilon = 10^{-4}$ the numerical results are compatible with $a = -1$. This dependence is consistent with CS production being purely a surface effect, which vanishes as $R_\star^{-1}$ in the physical limit of macroscopic bubbles (with $N_{\rm CS}$ produced only around the collision points). On the other hand, larger values of $\epsilon \gtrsim 0.2$ suggest a CS variance that becomes constant, $a = 0$, or grows, $a > 0$, in the physical limit of $m_h R_\star \to \infty$ and $\gamma_\star \to \infty$, as noticed before for $\epsilon = 0.32$. In the tested dynamical range, the CS variance from bubble collisions is smaller than the one from tachyonic instability with instantaneous quench by one or two orders of magnitude. However, we stress again that these results need to be extrapolated to the physical point with $\gamma_\star \gg 1$.

The regime $\epsilon \gtrsim 0.2$, where interestingly $N_{\rm CS}$ does not appear to decrease with $\gamma_\star$, is challenging to study numerically at $\gamma_\star \gg 1$ because R_c is parametrically larger than the wall width. Since we only test a relatively small range of $\gamma_\star$ and results have still quite large statistical uncertainties, the data does not allow us to reconstruct $\Delta n^2_{\rm CS}$ reliably at macroscopic $\gamma_\star$. In any case, for $\epsilon \gtrsim 0.3$ the data favors a growing variance $\Delta n^2_{\rm CS} \propto \gamma_\star^a$, with $a \gtrsim 1$. The best-fit values are $a \simeq 1.3(2)$ and $a \simeq 1.8(4)$ for $\epsilon = \{0.32, 0.45\}$, respectively. Taken together, these results suggest that $\Gamma_{\rm CS} \propto \gamma_\star^{a-1}$ is likely not volume suppressed at large $\gamma_\star$. Stronger evidence for this trend, possibly suggesting the value $a \simeq 1$, appears in the $(1+1)$D $U(1)$ gauge-field case (see Fig. 6 and the discussion in section Results from $(1+1)D$ simulations of Higgs bubble collisions of the End Matter), which probes larger ϵ and $\gamma_\star$. The numerical treatment of such $(1+1)$D system is discussed in more detail in Supplemental Material II [39]. Despite these limitations, to the best of our knowledge, this Letter

represents the current state of the art in real-time $(3+1)$D simulations of first-order PT in $SU(2)$ gauge theory [simulations of two-bubble collisions with(out) $U(1)$-gauge field have been carried out up to $\gamma_\star \sim 5$ in Ref. [46] ($\gamma_\star = 20$ in Ref. [45]), while multiple bubble collisions without gauge fields were simulated in $(3+1)$D with $\gamma_\star$ as large as $\gamma_\star \simeq 6$ in [47] and $\gamma_\star \simeq 50$ in $(1+1)$D in [44]].

Our main conclusion is that ϵ is a crucial parameter determining whether B can be produced over a large volume. If the vacua are highly nondegenerate (small ϵ), bubble collision is limited to the surfaces. Instead, for nearly degenerate vacua (large ϵ), walls pass through each other, extending the collision region and the production of $N_{\rm CS}$ far out from the initial point. CS transitions then extend to a sizable fraction of the whole volume due to the subsequent transfer of energy from the wall kinetic energy to other gauge and Higgs field configurations (see third panel of Fig. 1).

Chern-Simons variance from the spectrum—The CS number density spectrum $P_{\rm CS}(k)$ provides more detailed information on the length scales at which the CS number is produced. This is defined by $\langle n_{\rm CS}(k) n^*_{\rm CS}(k')\rangle = (2\pi)^3\delta^3(k-k')[2\pi^2/k^3]P_{\rm CS}(k)$, where $n_{\rm CS}(k) = \int d^3x e^{-ikx} n_{\rm CS}(x)$ and $N_{\rm CS} = \int d^3x n_{\rm CS}$. Since the field fluctuations are uncorrelated beyond the typical bubble separation, we expect $P_{\rm CS}(k)$ to have the white-noise behavior $P_{\rm CS}(k) = Ck^3/(2\pi^2)$ for $k \ll 2\pi/R_\star$. From Eqs. (1) and (2) one readily verifies that the coefficient C is in fact the CS variance, $C = \Delta n^2_{\rm CS}$, see Supplemental Material I [39].

Figure 4 shows power spectra for $\epsilon = \{10^{-2}, 0.45\}$ and $\gamma_\star = \{3, 6\}$. Most of the CS number is generated at scales of order m_h^{-1}, since both spectra peak at $k \simeq m_h$. However, for $\epsilon = 0.45$, the spectra also develop a small IR shoulder at $k \simeq 2\pi/R_\star$. This becomes increasingly pronounced as $\gamma_\star$ grows, at the expense of the m_h peak, which is progressively reduced at larger $\gamma_\star$. At lower momenta, the spectrum roughly follows the expected white-noise behavior. These properties of the CS spectrum are much clearer in our $(1+1)$D simulations, as shown in Fig. 6 in the End Matter and further detailed in Supplemental Material II [39]. Taken together, these results suggest that in the $\gamma_\star \gg 1$ limit, the CS spectrum peaks at $k \simeq 2\pi/R_\star$ for large ϵ; consequently, the coefficient $C = \Delta n^2_{\rm CS}$ grows with $\gamma_\star$, and the production occurs over macroscopic scales $\sim R_\star$. The IR shoulder is instead absent for $\epsilon = 10^{-2}$, explaining the different behavior for the CS variance with $\gamma_\star$ in Fig. 3 (right).

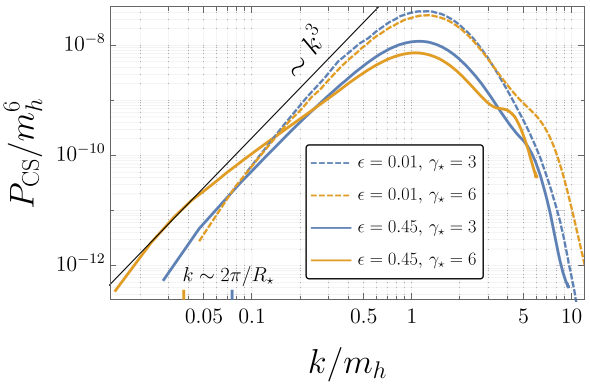


FIG. 4. Averaged CS number spectra for small and large ϵ, and for $\gamma_\star = \{3, 6\}$. For $\epsilon = 0.45$, the CS spectrum develops an IR shoulder at $k \sim 2\pi/R_\star$ (blue and orange ticks on the x axis), with a k^3 white-noise behavior at smaller k.

Estimate for the baryon asymmetry—This Letter computes a universal effect of the EW theory, which can have implications for a large range of Standard-Model extensions. In contrast, a baryon asymmetry calculation requires the introduction of CP-violating interactions and a model-dependent analysis. We can nevertheless argue how this new effect could lead to the correct baryon asymmetry. In a thermal environment, the baryon number density n_b obeys a Boltzmann equation that combines the rate of B violation Γ, the effect of CP violation in producing a net asymmetry μ, and washout terms $\mathcal{A}$: $(\partial/\partial t) n_b(x,t) = \Gamma(\xi - \mathcal{A} n_b)$, where $\xi \equiv \mu/T$ is the effective chemical potential for the baryons. Γ and μ are in general space-time dependent, while we will neglect $\mathcal{A}$ for simplicity. In standard electroweak baryogenesis (EWBG) for instance, the chemical potential is nonzero only in the vicinity of the expanding bubble, while sphalerons are active only in the symmetric phase ahead of the wall, $\Gamma = \Gamma_{\rm th}$. On the other hand, the scenario of cold baryogenesis introduced in Ref. [4] does not rely on a first-order PT for driving the system out of equilibrium, but rather on the tachyonic instability at the top of the SM Higgs potential. This dynamics can be considered homogeneous in space, at least over scales that are much larger than the typical size of the SM textures [8]. The baryon asymmetry can be estimated by referring to a volume-averaged sphaleron rate and chemical potential. The former is extracted from numerical simulations via the diffusion of the CS number, Eq. (1). CP violation is usually introduced via the following dimension-six operator [4,8,13] (see however [48] and [26] for other choices), $\mathcal{O} = (g^2/32\pi^2\Lambda^2)\phi^\dagger\phi W^a_{\mu\nu}\tilde{W}^{\mu\nu a}$, where Λ corresponds to the new physics scale at which $\mathcal{O}$ is generated. Current bounds on Λ are dominated by those from the electron electric dipole moment, see, e.g., Ref. [49], and lead to $\Lambda \gtrsim 6$ TeV. $\mathcal{O}$ generates an effective chemical potential $\mu = N_F^{-1}(1/\Lambda^2)[d/dt]\langle\phi^\dagger\phi\rangle$, as can be seen by integrating by parts $\int d^4x\mathcal{O}$ and taking volume averages, $\langle\ldots\rangle$, see, e.g., Refs. [4,50].

The scenario considered in this Letter is somewhat in between EWBG and the original cold baryogenesis setup, as it relies on a first-order EWPT but also on the subsequent dynamics leading to a reequilibration of the Higgs and gauge fields, as advocated in [25,26].

We may estimate the baryon asymmetry following the approach adopted in cold baryogenesis. We stress, however, that this estimate is based on volume-average quantities, and it may differ significantly in case the CS transitions are localized around the (collided) walls. By considering the same source of CP violation from the operator $\mathcal{O}$, we can derive the effective chemical potential by referring to Fig. 2 (left) and introducing the following parametrization for the Higgs average variance: $\langle|\phi|^2\rangle = (v^2/2)f(bt/R_\star)$, where $b \sim \mathcal{O}(1)$ accounts for a possibly different time scale compared to the CS variance in Eq. (3) (in fact, the Higgs norm converges faster than the CS variance). The total baryon asymmetry is then given by $n_b = \int dt \Gamma_{\rm CS}(t)\mu(t)/T_{\rm eff}(t)$, where $T_{\rm eff} = \Gamma_{\rm CS}^{1/4}/\alpha_w$. We then obtain for the baryon yield to entropy density ratio $n_b/s \simeq 10^{-10}\gamma_\star^{3(a-1)/4}(30\ {\rm GeV}/T_{\rm rh})^3(10\ {\rm TeV}/\Lambda)^2$, where $T_{\rm rh}$ is the reheat temperature after the EWPT. In deriving this expression we have taken $R_c = 10 m_h^{-1}$ as a typical value, and used that $(b/2)\int_0^\infty dx f'(x)f'(bx) \approx 0.1$. This estimate implies that $a \geq 1$ is required for successful baryogenesis (i.e., $n_b/s \gtrsim 10^{-10}$); otherwise, n_b/s is suppressed at large $\gamma_\star$. However, $a \geq 0$ may suffice if the CS transitions occur locally, following the motion of the walls after collision, as suggested by the $(1+1)$D case in Fig. 6 (bottom panel) in the End Matter. In this case the previous estimate based on volume-average quantities would not apply, and the convolution of a local CS rate with the regions where CP violation occurs may still lead to unsuppressed baryon asymmetry, similarly to EWBG. The analysis of the $(3+1)$D system including a dynamical CP-violating operator (e.g., $\mathcal{O}$) is however needed to ultimately establish the viable parameter space (e.g., ϵ and Λ) for successful cold baryogenesis. For such analysis, the key quantity will be the (nonzero) average $\langle N_{\rm CS}\rangle$, which is directly related to baryon number, rather than the variance $\langle N_{\rm CS}^2\rangle$ as considered here.

Conclusion—SM Higgs bubble collisions provide a new sizeable source of Chern-Simons number. We calculated from first-principles $(3+1)$D real-time simulations the corresponding CS rate in the runaway regime and showed its sensitivity on the shape of the scalar potential driving the first-order EWPT. For $\epsilon \gtrsim 0.3$, there is no volume suppression. The next step will be to implement CP violation on the lattice to evaluate precisely the net baryon number. This may provide an alternative realization of electroweak baryogenesis in the large bubble wall velocity limit, which does not rely on the charge transport mechanism. More generally, it will be important to investigate the impact of this potentially new washout effect on the standard EW baryogenesis mechanism. An interesting extension is to include the $U(1)$ gauge field and calculate magnetic-field production in the spirit of, e.g., [51–54]. These simulations can also predict the resulting gravitational-wave background.

Acknowledgments—We thank Anders Tranberg and Hyungjin Kim for discussions. This research was supported in part through the Maxwell computational resources operated at Deutsches Elektronen-Synchrotron DESY, Hamburg, Germany. This work, and M. C. in particular, is supported by the Deutsche Forschungsgemeinschaft under Germany's Excellence Strategy—EXC 2121 "Quantum Universe"—390833306. N. B. acknowledges support by the Deutsche Forschungsgemeinschaft (DFG, German Research Foundation) under the DFG Emmy Noether Grant No. PI 1933/1-1. The work of M. G. is supported by the Alexander von Humboldt foundation. G. S. thanks the theory group at Berkeley for hospitality in the very last stages of completion of this work as well as the European Union's Horizon Europe program under Marie Skłodowska-Curie Actions—Staff Exchanges Grant Agreement No. 101086085 -ASYMMETRY.

Data availability—The data that support the findings of this article are not publicly available. The data are available from the authors upon reasonable request.

[1] V. A. Kuzmin, V. A. Rubakov, and M. E. Shaposhnikov, On the anomalous electroweak baryon number nonconservation in the early universe, Phys. Lett. **155B**, 36 (1985).
[2] M. Fukugita and T. Yanagida, Baryogenesis Without grand unification, Phys. Lett. B **174**, 45 (1986).
[3] S. Davidson, E. Nardi, and Y. Nir, Leptogenesis, Phys. Rep. **466**, 105 (2008).
[4] J. Garcia-Bellido, D. Y. Grigoriev, A. Kusenko, and M. E. Shaposhnikov, Nonequilibrium electroweak baryogenesis from preheating after inflation, Phys. Rev. D **60**, 123504 (1999).
[5] L. M. Krauss and M. Trodden, Baryogenesis below the electroweak scale, Phys. Rev. Lett. **83**, 1502 (1999).
[6] J. M. Cornwall and A. Kusenko, Baryon number nonconservation and phase transitions at preheating, Phys. Rev. D **61**, 103510 (2000).
[7] E. J. Copeland, D. Lyth, A. Rajantie, and M. Trodden, Hybrid inflation and baryogenesis at the TeV scale, Phys. Rev. D **64**, 043506 (2001).
[8] J. Garcia-Bellido, M. Garcia-Perez, and A. Gonzalez-Arroyo, Chern-Simons production during preheating in hybrid inflation models, Phys. Rev. D **69**, 023504 (2004).
[9] K. Enqvist, P. Stephens, O. Taanila, and A. Tranberg, Fast electroweak symmetry breaking and cold electroweak baryogenesis, J. Cosmol. Astropart. Phys. 09 (2010) 019.
[10] J. Smit and A. Tranberg, Chern-Simons number asymmetry from CP violation at electroweak tachyonic preheating, J. High Energy Phys. 12 (2002) 020.
[11] A. Tranberg and J. Smit, Baryon asymmetry from electroweak tachyonic preheating, J. High Energy Phys. 11 (2003) 016.
[12] M. van der Meulen, D. Sexty, J. Smit, and A. Tranberg, Chern-Simons and winding number in a tachyonic electroweak transition, J. High Energy Phys. 02 (2006) 029.

[13] A. Tranberg and J. Smit, Simulations of cold electroweak baryogenesis: Dependence on Higgs mass and strength of CP-violation, J. High Energy Phys. 08 (2006) 012.
[14] A. Tranberg, J. Smit, and M. Hindmarsh, Simulations of cold electroweak baryogenesis: Finite time quenches, J. High Energy Phys. 01 (2007) 034.
[15] A. Tranberg, Standard model CP-violation and cold electroweak baryogenesis, Phys. Rev. D **84**, 083516 (2011).
[16] A. Tranberg and B. Wu, Cold electroweak baryogenesis in the two Higgs-doublet model, J. High Energy Phys. 07 (2012) 087.
[17] Z.-G. Mou, P. M. Saffin, and A. Tranberg, Cold baryogenesis from first principles in the two-Higgs doublet model with fermions, J. High Energy Phys. 06 (2015) 163.
[18] Z.-G. Mou, P. M. Saffin, and A. Tranberg, Simulations of cold electroweak baryogenesis: Finding the optimal quench time, J. High Energy Phys. 07 (2017) 010.
[19] Z.-G. Mou, P. M. Saffin, and A. Tranberg, Simulations of cold electroweak baryogenesis: Hypercharge U(1) and the creation of helical magnetic fields, J. High Energy Phys. 06 (2017) 075.
[20] Z.-G. Mou, P. M. Saffin, and A. Tranberg, Simulations of cold electroweak baryogenesis: Quench from portal coupling to new singlet field, J. High Energy Phys. 01 (2018) 103.
[21] Z.-G. Mou, P. M. Saffin, and A. Tranberg, Simulations of cold electroweak baryogenesis: Dependence on the source of *CP*-violation, J. High Energy Phys. 05 (2018) 197.
[22] M. D'Onofrio, K. Rummukainen, and A. Tranberg, Sphaleron rate in the minimal standard model, Phys. Rev. Lett. **113**, 141602 (2014).
[23] G. C. Dorsch, S. J. Huber, and T. Konstandin, On the wall velocity dependence of electroweak baryogenesis, J. Cosmol. Astropart. Phys. 08 (2021) 020.
[24] T. Konstandin and G. Servant, Cosmological consequences of nearly conformal dynamics at the TeV scale, J. Cosmol. Astropart. Phys. 12 (2011) 009.
[25] T. Konstandin and G. Servant, Natural cold baryogenesis from strongly interacting electroweak symmetry breaking, J. Cosmol. Astropart. Phys. 07 (2011) 024.
[26] G. Servant, Baryogenesis from strong *CP* violation and the QCD Axion, Phys. Rev. Lett. **113**, 171803 (2014).
[27] B. von Harling and G. Servant, Cosmological evolution of Yukawa couplings: The 5D perspective, J. High Energy Phys. 05 (2017) 077.
[28] S. Bruggisser, B. Von Harling, O. Matsedonskyi, and G. Servant, Electroweak phase transition and baryogenesis in composite Higgs models, J. High Energy Phys. 12 (2018) 099.
[29] S. Bruggisser, B. von Harling, O. Matsedonskyi, and G. Servant, Status of electroweak baryogenesis in minimal composite Higgs, J. High Energy Phys. 08 (2023) 012.
[30] S. Bruggisser, B. von Harling, O. Matsedonskyi, and G. Servant, Dilaton at the LHC: Complementary probe of composite Higgs, J. High Energy Phys. 05 (2023) 080.
[31] I. Baldes, S. Blasi, A. Mariotti, A. Sevrin, and K. Turbang, Baryogenesis via relativistic bubble expansion, Phys. Rev. D **104**, 115029 (2021).
[32] A. Azatov, M. Vanvlasselaer, and W. Yin, Baryogenesis via relativistic bubble walls, J. High Energy Phys. 10 (2021) 043.
[33] M. Dichtl, J. Nava, S. Pascoli, and F. Sala, Baryogenesis and leptogenesis from supercooled confinement, J. High Energy Phys. 02 (2024) 059.
[34] M. Cataldi and B. Shakya, Leptogenesis via bubble collisions, J. Cosmol. Astropart. Phys. 11 (2024) 047.
[35] N. Turok and J. Zadrozny, Electroweak baryogenesis in the two doublet model, Nucl. Phys. **B358**, 471 (1991).
[36] G. D. Moore, The Sphaleron rate: Where we stand, in *3rd International Conference on Strong and Electroweak Matter*, (1998), pp. 23–33, arXiv:hep-ph/9902464.
[37] G. D. Moore, Do we understand the Sphaleron rate?, in *4th International Conference on Strong and Electroweak Matter*, (2000), pp. 82–94, arXiv:hep-ph/0009161.
[38] https://www.youtube.com/watch?v=LhZFCxJ5-4g.
[39] See Supplemental Material at http://link.aps.org/supplemental/10.1103/fv7q-vsbn for more details regarding our model implementation and numerical procedure.
[40] C. Grojean, G. Servant, and J. D. Wells, First-order electroweak phase transition in the standard model with a low cutoff, Phys. Rev. D **71**, 036001 (2005).
[41] C. Delaunay, C. Grojean, and J. D. Wells, Dynamics of non-renormalizable electroweak symmetry breaking, J. High Energy Phys. 04 (2008) 029.
[42] J. de Vries, M. Postma, J. van de Vis, and G. White, Electroweak baryogenesis and the standard model effective field theory, J. High Energy Phys. 01 (2018) 089.
[43] D. G. Figueroa, A. Florio, F. Torrenti, and W. Valkenburg, The art of simulating the early Universe—Part I, J. Cosmol. Astropart. Phys. 04 (2021) 035.
[44] R. Jinno, T. Konstandin, and M. Takimoto, Relativistic bubble collisions—a closer look, J. Cosmol. Astropart. Phys. 09 (2019) 035.
[45] O. Gould, S. Sukuvaara, and D. Weir, Vacuum bubble collisions: From microphysics to gravitational waves, Phys. Rev. D **104**, 075039 (2021).
[46] M. Lewicki and V. Vaskonen, Gravitational waves from colliding vacuum bubbles in gauge theories, Eur. Phys. J. C **81**, 437 (2021).
[47] D. Cutting, M. Hindmarsh, and D. J. Weir, Gravitational waves from vacuum first-order phase transitions: From the envelope to the lattice, Phys. Rev. D **97**, 123513 (2018).
[48] A. Tranberg, A. Hernandez, T. Konstandin, and M. G. Schmidt, Cold electroweak baryogenesis with standard model *CP* violation, Phys. Lett. B **690**, 207 (2010).
[49] V. Cirigliano, A. Crivellin, W. Dekens, J. de Vries, M. Hoferichter, and E. Mereghetti, CP Violation in Higgs-Gauge Interactions: From tabletop experiments to the LHC, Phys. Rev. Lett. **123**, 051801 (2019).
[50] M. Dine, P. Huet, and R. L. Singleton, Jr., Baryogenesis at the electroweak scale, Nucl. Phys. **B375**, 625 (1992).
[51] T. Vachaspati and A. Brandenburg, Spectra of magnetic fields from electroweak symmetry breaking, Phys. Rev. D **111**, 043541 (2025).
[52] Y. Di, J. Wang, R. Zhou, L. Bian, R.-G. Cai, and J. Liu, Magnetic field and gravitational waves from the first-order phase transition, Phys. Rev. Lett. **126**, 251102 (2021).

[53] Y. Di, L. Bian, and R.-G. Cai, Baryogenesis induced by magnetic field effects during the electroweak phase transition, arxiv:2409.16124.
[54] Y. Di, L. Bian, and R.-G. Cai, Impact of primordial magnetic fields on the first-order electroweak phase transition, Phys. Rev. D **113**, 043529 (2026).
[55] D. Bodeker and G. D. Moore, Can electroweak bubble walls run away?, J. Cosmol. Astropart. Phys. 05 (2009) 009.
[56] D. Bodeker and G. D. Moore, Electroweak bubble wall speed limit, J. Cosmol. Astropart. Phys. 05 (2017) 025.
[57] Y. Gouttenoire, R. Jinno, and F. Sala, Friction pressure on relativistic bubble walls, J. High Energy Phys. 05 (2022) 004.
[58] A. Azatov and M. Vanvlasselaer, Bubble wall velocity: Heavy physics effects, J. Cosmol. Astropart. Phys. 01 (2021) 058.
[59] A. Azatov, G. Barni, R. Petrossian-Byrne, and M. Vanvlasselaer, Quantisation across bubble walls and friction, J. High Energy Phys. 05 (2024) 294.
[60] I. Baldes, M. Dichtl, Y. Gouttenoire, and F. Sala, Particle shells from relativistic bubble walls, J. High Energy Phys. 07 (2024) 231.
[61] S. Blasi and A. Mariotti, Domain walls seeding the electroweak phase transition, Phys. Rev. Lett. **129**, 261303 (2022).
[62] P. Agrawal, S. Blasi, A. Mariotti, and M. Nee, Electroweak phase transition with a double well done doubly well, J. High Energy Phys. 06 (2024) 089.
[63] S. Blasi, R. Jinno, T. Konstandin, H. Rubira, and I. Stomberg, Gravitational waves from defect-driven phase transitions: Domain walls, J. Cosmol. Astropart. Phys. 10 (2023) 051.

End Matter

Winding and CS number—In Fig. 5 we show the evolution of the winding number and the CS number during the collision of three (left panel) and two (right panel) runaway bubbles. The two quantities converge at the end of the EWPT, as expected for vacuum configurations where indeed $N_{\rm CS} = N_W$. This represents a nontrivial cross check of our numerical simulations, and shows how winding configurations play a crucial role in triggering CS transitions. Bubble collisions initially generate a nonvanishing N_W, after which $N_{\rm CS}$ asymptotes toward N_W. However, $N_{\rm CS}$ does not coincide exactly with N_W, since part of the Chern-Simons number can be carried away by propagating W-boson waves. Conversely, we have checked that the collision of two bubbles leads to identically vanishing N_W due to the axial symmetry, and we have consistently observed that the total CS number is $N_{\rm CS} \ll 1$ oscillating around zero. This behavior can actually be seen in the first snapshot of Fig. 1, where a two-bubble collision produces approximately equal and opposite CS number density.

Runaway bubbles—As mentioned in the main text, our simulations apply to electroweak bubbles that collide in the runaway regime. For this case to be physically realized, the vacuum pressure given by the zero-temperature potential needs to overcome the friction from particles gaining mass across the wall in the ballistic regime [55]. Moreover, the boost factor at collision, $\gamma_\star$, needs to be smaller than the one

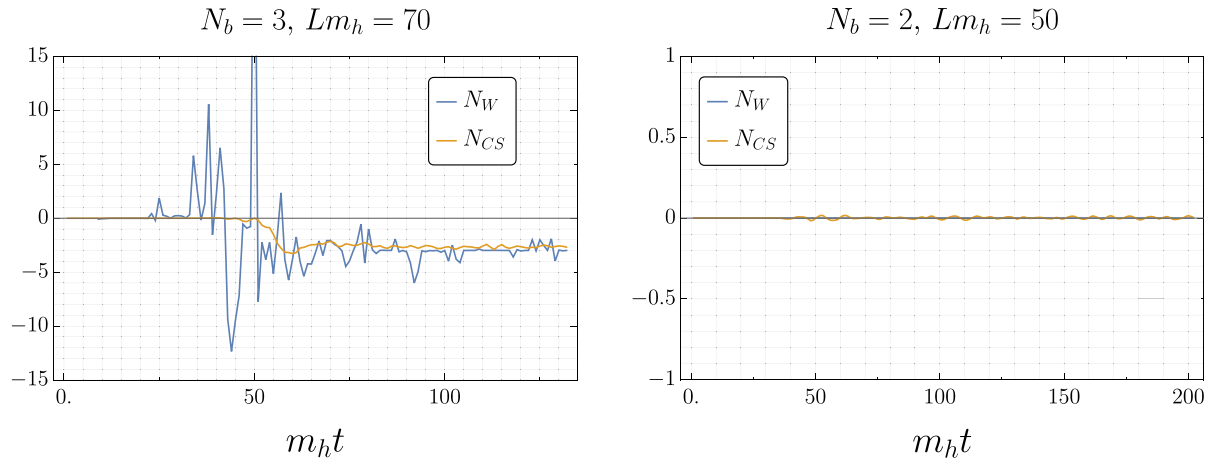


FIG. 5. Evolution of the winding and Chern-Simons numbers N_W and $N_{\rm CS}$ from a three-bubble collision (left panel), and a two-bubble collision (right panel) for $\epsilon = 0.2$ in $(3+1)$D. For $N_b = 3$, N_W is produced as bubbles collide, while for $N_b = 2$, $N_W \equiv 0$ because of the symmetry of the system. While locally $n_{\rm CS}$ is large as shown in the symmetric blue and red arches in the bottom-right two-bubble collision of the first snapshot of Fig. 1, once integrated over the volume, $N_{\rm CS}$ is suppressed for $N_b = 2$. In both cases, $N_{\rm CS}$ asymptotically relaxes to N_W as expected in a vacuum configuration.

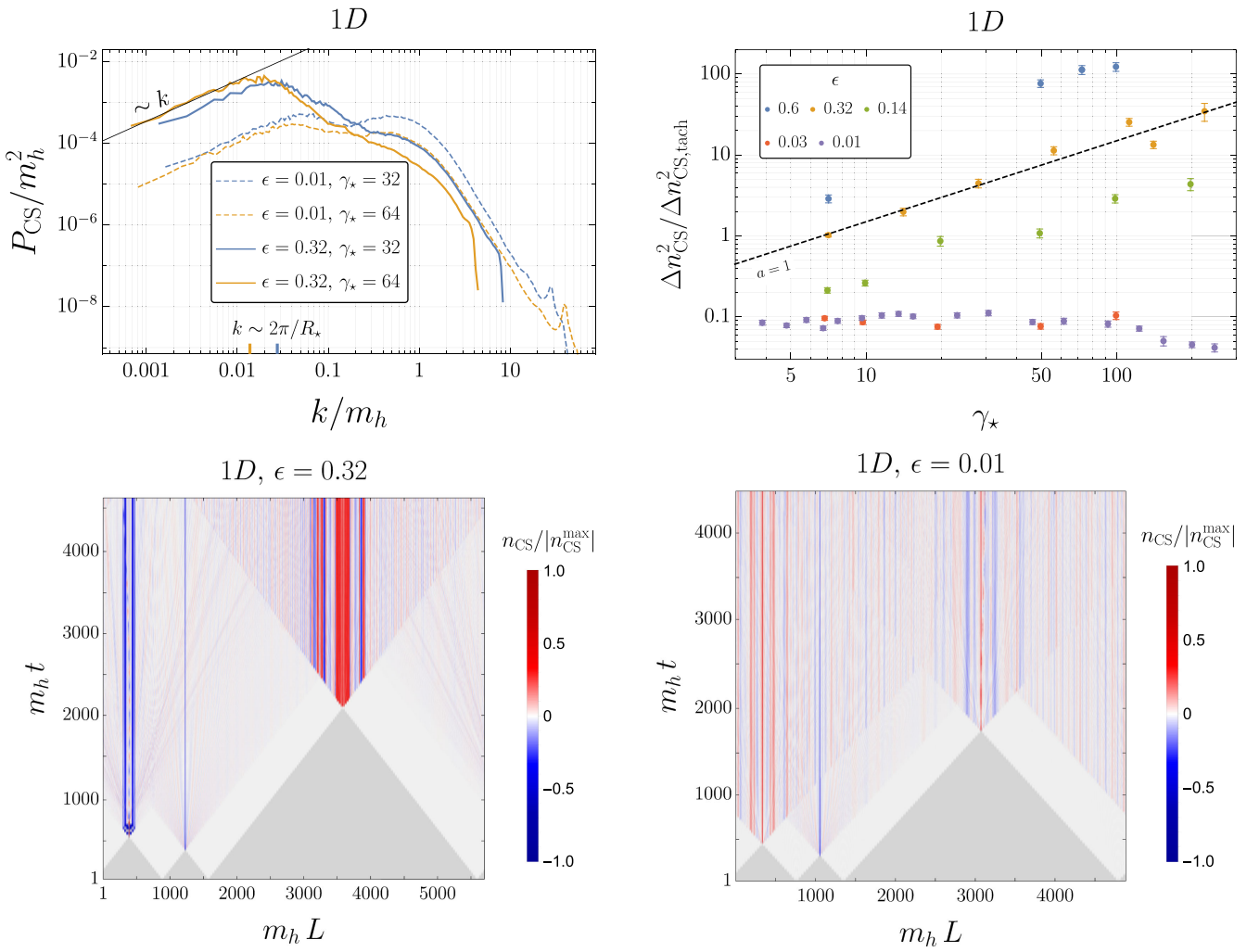


FIG. 6. $(1+1)$D simulations. Top panel, left: the power spectrum of $n_{\rm CS}$, for small and large degeneracy parameter, $\epsilon = \{0.01, 0.32\}$. The power spectrum peaks at the scale corresponding to bubble radius at collision $R_\star$, i.e., momentum $2\pi/R_\star$ (blue and orange ticks on the x axis). For $\epsilon = 0.32$, the coefficient of the IR slope at $k < 2\pi/R_\star$ (proportional to $n^2_{\rm CS}$) is higher at larger $\gamma_\star$, indicating an (approximately linear) increase in $n^2_{\rm CS}$ for increasing $\gamma_\star$. Top panel, right: CS variance (averaged over 100 realizations) as a function of $\gamma_\star$, for different values of ϵ, normalized by that produced in a tachyonic transition with instantaneous quench, $\Delta n^2_{\rm CS,tach} = 0.4 m_h$. Bottom panel: time evolution of a three-bubble collision, with $\epsilon = 0.32$ (left), 0.01 (right). The unbroken phase is represented by dark gray region, while the broken one by light gray. The CS number density is shown in blue and red, normalized to its maximal value attained in the simulation.

corresponding to the terminal velocity imposed by balancing the next-to-leading order pressure from particle splitting, $\mathcal{P}_{\rm NLO} \sim \alpha_w \gamma_w m_W T_n^3$ [56] (see also Refs. [57–60] for recent work), where T_n is the nucleation temperature, with $\Delta V \sim v^4$, as typical for a supercooled phase transition. Runaway collisions take place then if $\gamma_w \sim 4\pi^2 (v/gT_n)^3$ is larger than $\gamma_\star = R_\star/R_c \sim v R_\star$, with $R_\star \simeq (8\pi)^{1/3} \beta^{-1} v_w$. Taking $H \sim v^2/M_{\rm Pl}$ for the Hubble expansion, one obtains $\beta/H \gtrsim 0.1 (T_n/{\rm MeV})^3$. This condition may be satisfied for low nucleation temperatures or large values of β/H, i.e., for fast phase transitions. For instance, $T_n \sim 10$ MeV requires $\beta/H \sim 10^2$, while $T_n \in [0.1 - 1]$ GeV leads to $\beta/H \in [10^5 – 10^8]$. The latter (large) values of β/H could in fact be realized in scenarios with a seeded electroweak phase transition as explored in Refs. [61–63], where β/H is effectively replaced by the number of defects in the Hubble volume at the time of bubble nucleation, ξ, which can be as large as $\xi \sim 10^8$ for a domain wall network in the friction-dominated regime at the electroweak scale.

Results from $(1+1)D$ simulations of Higgs bubble collisions—To explore large collision boost factors, $\gamma_\star \gtrsim \mathcal{O}(10)$, desirable for extrapolation to the physical point, as well as scalar potentials with $\epsilon \gtrsim 0.1$ that

produce large critical bubbles, we performed simulations of runaway bubbles in $(1+1)$D. These significantly reduce computational cost compared to the $(3+1)$D simulations presented in the main text, allowing us to extend the simulation box more efficiently. For our $(1+1)$D simulations we have considered the Abelian Higgs model with a spontaneously broken $U(1)$ gauge symmetry already adopted in Ref. [4], as this captures the main topological properties of the SM in $(3+1)$D. The Higgs potential is modified in order to have a first order phase transition, and we have implemented a scalar potential analogue to the one used in the $(3+1)$D simulations, as presented in Supplemental Material I [39].

Our main results are displayed in Fig. 6. As shown in the top-left panel, the CS power spectrum exhibits markedly different IR behavior depending on ϵ. For $\epsilon = 0.32$ (solid lines), a peak appears at $k \sim 2\pi/R_\star$, which shifts toward the IR as collisions go from $\gamma_\star = 32$ to $\gamma_\star = 64$, consistently tracking $2\pi/R_\star$ (recall that $R_\star/R_c = \gamma_\star$). Since the CS variance is proportional to the amplitude of the IR tail at $k \ll 2\pi/R_\star$, which scales as $\propto k$ by causality in $(1+1)$D, the CS variance is observed to increase with $\gamma_\star$ (top-right panel of Fig. 6). In contrast, for $\epsilon = 0.01$, the IR power spectrum does not increase with $\gamma_\star$, leading to a constant or decreasing CS variance. As in $(3+1)$D, a smaller and smaller peak appears at $k \sim m_h$, but it does not contribute to the CS variance.

Despite the clear differences between the $(1+1)$D and $(3+1)$D systems, the Higgs potential shape, encoded in ϵ, strongly influences CS production in both cases. In $(1+1)$D, the variance is significantly larger than that from the tachyonic instability and grows approximately linearly with $\gamma_\star$, as indicated by the $a = 1$ line in the top-right panel of Fig. 6 [using the same parametrization of Eq. (3) for the CS variance]. Whether such linear growth occurs in $(3+1)$D remains an open question.

Finally, we comment on the spatial dependence of CS transitions in this lower-dimensional setup, as seen in the bottom panel of Fig. 6. CS number appears to be predominantly produced along the trajectories of collided bubble walls and is not reprocessed afterward. This corresponds to straight lines along the time direction with the same value of the CS number density, $n_{\rm CS}$. Since the collided walls eventually sweep an $\mathcal{O}(1)$ fraction of the volume, CS production is not purely a surface effect. The $(3+1)$D analog of Fig. 6 (bottom panel), namely Fig. 1, shows a less clear indication for the spatial dependence of the CS production (i.e., whether it follows precisely the collided walls), but we expect that similar dynamics may take place in $(3+1)$D. Additionally, for $\epsilon = 0.32$ (left panel), regions with sizable CS number are much wider than for $\epsilon = 0.01$ (right panel). For $\epsilon = 0.32$ one can also notice the reformation of pockets of the false vacuum after the initial collision, as seen for the leftmost collision in the bottom panel of Fig. 6 (left).